

Photocatalytic streamlined dual-functional group transfer from cyanopyridine to internal alkynes

Received: 13 May 2025

Accepted: 7 September 2025

Published online: 09 October 2025



Xiaogang Tong^{1,2,4}, Jialong Jie^{3,4}, Yan Liu³, Haihan Yu¹, Mingquan Yuan¹,
Hwee Ting Ang², Gan Wang², Duanshuai Tian², Hongmei Su³✉ &
Jie Wu²✉

The streamlined dual-functional group transfer (streamlined dual-FGT) strategy represents an efficient and sustainable approach for difunctionalization reactions, where all atoms or functional groups from the starting materials are fully incorporated into the final products without generating by-products. Pyridine and nitrile functionalities are prevalent and highly valued structural motifs found in a myriad of natural products, pharmaceuticals, agrochemicals, and polymers. The simultaneous incorporation of these groups via the streamlined dual-FGT strategy is thus of considerable significance in synthetic chemistry. Herein, we report a regioselective pyridylcyanation of internal alkynes enabled by an oxalate-based photocatalytic system, employing cyanopyridine as a streamlined dual-functional group transfer reagent. Mechanistic investigations using time-resolved spectroscopy reveal that the transformation proceeds through a photoinduced regioselective radical addition of the persistent cyanopyridine radical anion to alkynes, followed by the cooperative release and re-addition of the cyanide ion (CN⁻).

In the realm of modern organic synthesis, the development of highly selective, step- and atom-economical, and environmentally sustainable transformations remains a central objective^{1,2}. Functional group transfer reactions have emerged as powerful tools, enabling the direct transfer of specific atoms or functional groups from one molecule to another^{3–7}. The difunctionalization of alkenes^{8–12} and alkynes^{13–15} has proven particularly valuable, offering an efficient approach to introduce two functional groups in a single step, thereby enhancing molecular complexity. Among these strategies, three-component difunctionalization reactions employing two mono-functional group transfer reagents (mono-FGTRs) are well-established, primarily due to the broad availability and structural diversity of these reagents. However, their utility is often limited by suboptimal atom economy and the generation of considerable by-products^{16–18}. Recent years have witnessed a growing interest in the development of bridged dual-

functional group transfer reagents (bridged dual-FGTRs), aiming to enhance reaction efficiency and atom economy by transferring two functional groups from a single reagent. Nevertheless, their broader application remains challenging due to limited reagent accessibility and by-products formation^{19–25}. In contrast, difunctionalization reactions employing streamlined dual-functional group transfer reagents (streamlined dual-FGTRs) achieve 100% atom economy with no by-products formation^{26,27}, offering a more sustainable alternative that aligns closely with the principles of green chemistry (Fig. 1a).

Pyridine^{28–30} and nitrile^{31,32} groups are prevalent structural motifs in pharmaceuticals, natural products, agrochemicals, and polymers. In medicinal chemistry, pyridine derivatives exhibit various important pharmacological activities such as antimicrobial, antimalarial, anti-diabetic, and anti-inflammatory^{28,33}, while the nitrile group is an excellent ligand for protein binding due to its high polarity, small size,

¹School of Chemical Science and Technology, Yunnan University, Kunming, PR China. ²Department of Chemistry, National University of Singapore, Singapore, Singapore. ³College of Chemistry, Beijing Normal University, Beijing, PR China. ⁴These authors contributed equally: Xiaogang Tong, Jialong Jie. ✉e-mail: hongmei@bnu.edu.cn; chmjie@nus.edu.sg

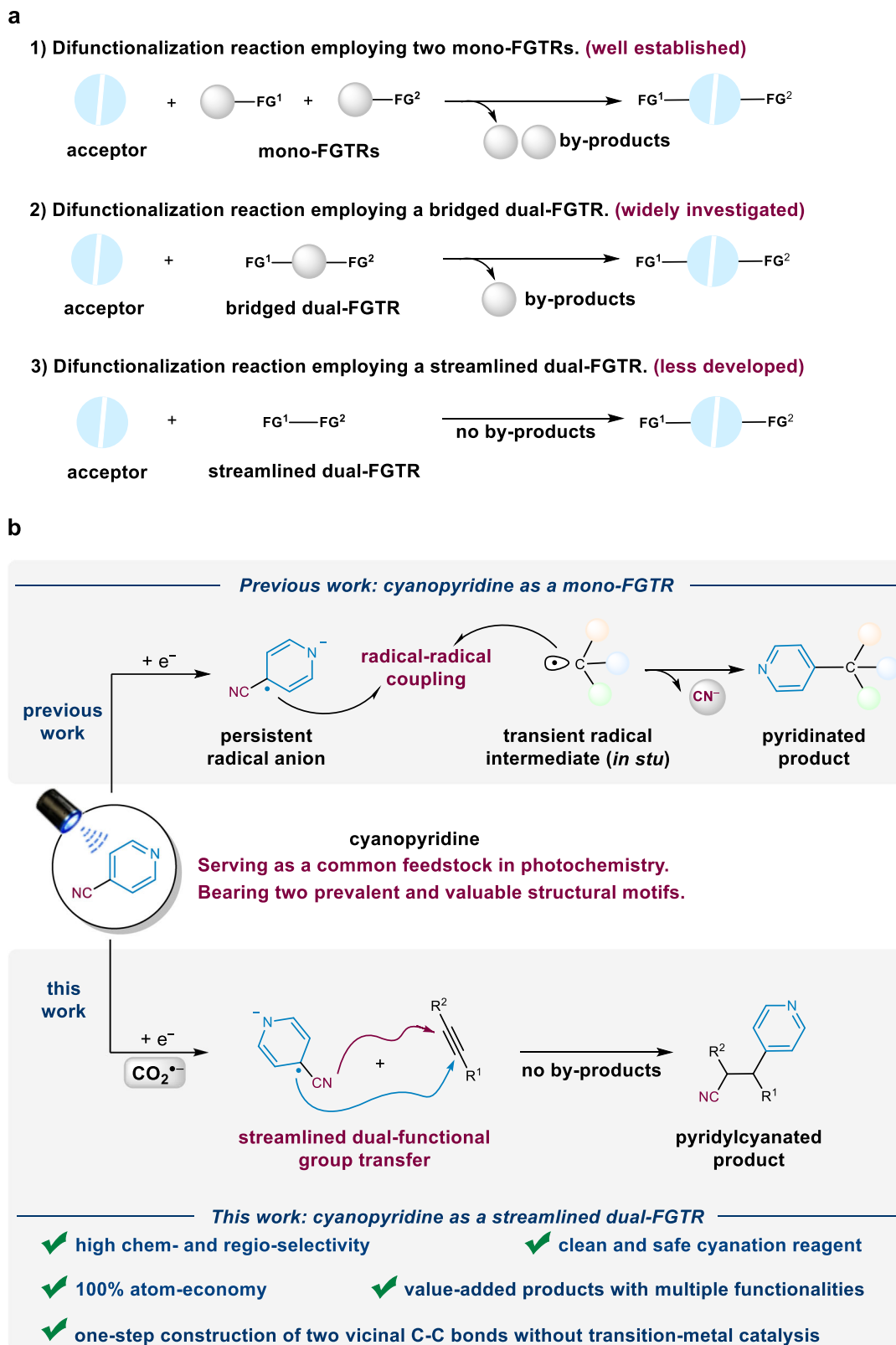


Fig. 1 | Project overview. **a** Strategies for difunctionalization reactions. **b** Cyanopyridine as a FGTR in photocatalysis. FG Functional Group, FGTR Functional Group Transfer Reagent.

linear geometry, metabolic stability, and capacity to accept hydrogen bonds³⁴. Both groups also exhibit remarkable synthetic versatility: pyridines can be readily reduced to piperidines³⁵, while nitriles can be transformed into a range of functional groups such as amines, amides, carboxylic acids/esters, aldehydes, and ketones^{36,37}. Consequently, the

development of efficient methods for the simultaneous incorporation of both pyridine and nitrile groups into organic molecules is of significant value. Recent advances in photochemistry have established cyanopyridine as a practical mono-FGTR for the synthesis of pyridine derivatives (Fig. 1b). Pioneering work by MacMillan and co-workers

demonstrated its utility in photocatalytic direct α -amino and allylic C–H pyridination^{38,39}. It has also been adopted in three-component 1,2-difunctionalization of alkenes, enabling the rapid assembly of structurally diverse pyridinated products^{40–46}. In such reactions, cyanopyridine typically undergoes single-electron reduction to form a persistent radical anion, which then couples with the in situ transient radical intermediate, allowing for the incorporation of the pyridine moiety while liberating the cyano group as a cyanide by-product^{47–49}. However, the direct introduction of nitrile groups remains challenging due to the hazardous nature of conventional cyanide sources, such as KCN, NaCN, CuCN, Zn(CN)₂, and K₄[Fe(CN)₆], which often release toxic hydrogen cyanide (HCN) during reactions. Therefore, strategies that enable the capture and incorporation of the cyano by-product into the final product hold significant promise. Such approaches could effectively transform cyanopyridine into a dual-FGTR, offering a more efficient, greener, and safer route for constructing complex molecules containing both pyridine and nitrile functionalities.

Alkynes are highly versatile building blocks in organic synthesis, and their reductive difunctionalization offers a powerful and cost-efficient approach to increasing molecular complexity. Building on our recent studies on the photocatalytic reductive hydroalkylation, arylalkenylation, and hydrocarboxylation of aryl alkynes via alkyne radical anions generated through an oxalate-based photocatalytic system^{50,51}, we aimed to develop a difunctionalization reaction involving cyanopyridine through a streamlined dual-FGT strategy. However, several challenges remain: (1) The inherently low reactivity of alkynes makes the one-step construction of two vicinal C–C bonds without transition-metal catalysis particularly challenging^{52–54}; (2) Achieving high regioselectivity in the difunctionalization of asymmetric alkynes remains a significant hurdle. Herein, we report the use of commercially available cyanopyridine as a streamlined dual-FGTR, enabling the regioselective pyridylcyanation of internal alkynes under visible-light irradiation (Fig. 1b). This method enables the direct construction of two vicinal C–C bonds on internal alkynes, providing an efficient strategy for the rapid assembly of pharmaceutical motifs and value-added products.

Results and discussion

Optimization of the reaction conditions

Inspired by Wen's work, methyl phenylpropiolate **1a** featuring an aryl and electron-withdrawing group (EWG) was employed as the model alkyne substrate⁵⁵. The proposed streamlined dual-FGT with 4-cyanopyridine **2a** was investigated under 30 W blue LED irradiation at room temperature (Table 1). Following extensive optimization, the pyridylcyanation product **3aa** was obtained in a 91% isolated yield with a 1.17:1 diastereomeric ratio (d.r.) using 2,4,5,6-tetrakis(diphenylamino)-1,3-dicyanobenzene (4DPAIPN) as a photocatalyst, in the presence of oxalic acid (H₂C₂O₄) and 1,1,3,3-tetramethylguanidine (TMG) in DMSO (Table 1, entry 1). The structure of **3aa** was unambiguously confirmed through X-ray crystallographic analysis. Unlike conventional transition-metal catalysis^{56–59}, our method overrides the inherent electronic bias, selectively installing the pyridyl group at the α -position of methyl phenylpropiolate **1a**, leading to the highly regioselective product **3aa**⁵⁵. Comparative evaluation of various photocatalysts, including [Ru(bpy)₃](PF₆)₂, [Ir(ppy)₂(dtbbpy)](PF₆), [Ir(dF(CF₃)ppy)₂(dtbbpy)](PF₆), and 2,4,5,6-tetrakis(carbazol-9-yl)-1,3-dicyanobenzene (4CzIPN), revealed significantly decreased yields of **3aa** (entries 2–5), likely due to the less favorable reduction potentials of their corresponding radical anions compared to 4DPAIPN[–], which facilitates the key single-electron transfer step⁵¹. Solvent screening showed that *N,N*-dimethylformamide (DMF) failed to initiate the reaction, while acetonitrile (MeCN) produced **3aa** in a modest 49% yield (entries 6 and 7). Replacing the H₂C₂O₄/TMG mixture with Na₂C₂O₄ or K₂C₂O₄ did not yield **3aa** (entry 8), whereas tetrabutylammonium oxalate ((ⁿBu₄N)₂C₂O₄) provided **3aa** in 56% yield (entry 9). These outcomes are likely due to the distinct solubility

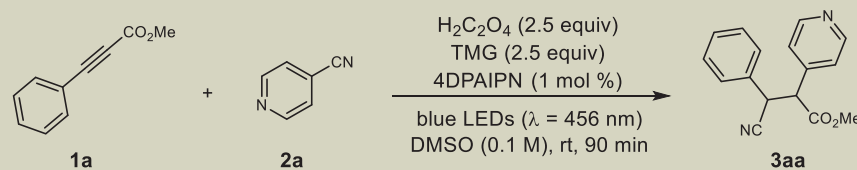
profiles of these oxalates in DMSO. Further evaluation of alternative reductants revealed that neither conventional sacrificial amine-based systems (e.g., Et₃N or *N,N*-diisopropylethylamine (DIPEA)) nor substitution of oxalic acid with formic acid could produce **3aa** (entries 10 and 11). These observations demonstrated the indispensable role of CO₂ radical anion (CO₂^{•–}), generated through single-electron transfer (SET) oxidation of oxalate, in facilitating this transformation. Moreover, we tested green LED (λ_{max} = 525 nm) and red LED (λ_{max} = 640 nm) light source under standard reaction conditions. Green light irradiation yielded **3aa** in 47% yield, while red light failed to initiate the reaction (entries 12 and 13). This aligns with 4DPAIPN's UV–vis absorption spectrum showing significant absorption in the blue light region, a weaker tail in the green light region, and negligible absorption in the red light region (Supplementary Fig. 6). Control experiments confirmed that no reaction occurred in the absence of light or photocatalyst (entries 14 and 15), underscoring their essential roles. Additionally, a sensitivity assessment based on reaction condition variations, commonly conducted to verify reproducibility⁶⁰, demonstrated that the transformation is oxygen-sensitive but generally robust to other perturbations (Supplementary Tables 1 and 2).

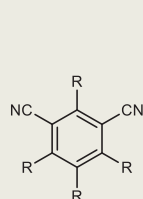
Substrate scope

With optimal reaction conditions established, the substrate scope was subsequently investigated. The yields depicted in Fig. 2 are isolated yields, with the d.r. varying between 1:1 and 2:1 (see the characterization of products in Supplementary Information for details). The scope of internal alkynes **1** was systematically evaluated first. To our delight, a wide range of ethyl 3-arylpropiolates **1** were viable substrates, delivering the desired products in good to excellent yields. Both electron-donating (e.g., alkyl, alkoxyl, and phenyl) and electron-withdrawing (e.g., fluoro, chloro, alkynyl, trifluoromethyl, and trifluoromethoxyl) substituents on the benzene moiety (**1b–1j**) were tolerated without a substantial impact on the reaction efficiency, affording the corresponding products in high yields (71–87%). Notably, our protocol exhibited remarkable chem- and regio-selectivity for arylpropiolate moiety, leading to the desired products **3ea** and **3fa** in 73% and 76% yield, respectively, while preserving the triple bonds of terminal alkyne (**3ea**) and diphenylacetylene (**3fa**) for subsequent transformations. These results demonstrated that both the aryl and ester groups on the alkynes were critical for driving the reaction with high regioselectivity. In addition, sterically demanding disubstituted and cyclic phenylpropiolate substrates with heteroatom substituents (**1k–1n**) were viable under standard conditions, affording the corresponding products in high yields. Other (hetero)aryl groups, including naphthyl, thiophene, and pyridyl (**1o–1t**), also reacted smoothly, albeit with slightly lower yields compared to phenylpropiolate substrates.

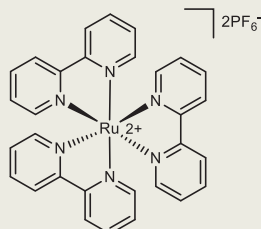
Moreover, the reaction was successfully applied to a series of phenylpropiolate esters bearing different functionalities such as phenyl (**3a'a**), pyridine (**3b'a**), pyrazole (**3c'a**), thiophene (**3d'a** and **3e'a**), ether, chloride (**3f'a**), silane (**3g'a**), terminal alkyne (**3h'a**), as well as ketal (**3i'a**). This protocol not only tolerated a wide range of functional groups but also retained stereocenters without racemization. For instance, the complex chiral substrate **1i'** was compatible with our mild reaction conditions, yielding product **3i'a** in 75% yield. The scope of cyanopyridine **2** was also evaluated using methyl phenylpropiolate **1a** as the alkyne substrate. As shown in Fig. 2, cyanopyridine substrates with diverse alkyl substituent groups, such as methyl (**3ab**, **3ac**, and **3aj**), benzyl (**3ad**), and sterically hindered *tert*-butyl (**3ae**), gave the desired products in high yields. Additionally, radical-sensitive strained cyclopropyl and cyclobutyl groups were tolerated under our reaction conditions (**3af** and **3ag**). Good yields of products were also obtained from the corresponding substrates possessing different functional motifs, such as cyclopentene (**2h**) and 1,1-difluorocyclohexane (**2i**). Unfortunately, neither 2-cyanopyridine (**2k**) nor 3-cyanopyridine (**2l**) was effective in our reaction system due to their more negative

Table 1 | Optimization of the reaction conditions^a

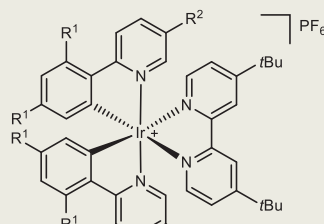
		
Entry	Variations from standard conditions	Yield of 3aa (%) ^b
1	none	94 (91) ^c
2	[Ru(bpy) ₃](PF ₆) ₂ instead of 4DPAIPN	36
3	[Ir(ppy) ₂ (dtbbpy)](PF ₆) instead of 4DPAIPN	78
4	[Ir(dF(CF ₃)ppy) ₂ (dtbbpy)](PF ₆) instead of 4DPAIPN	54
5	4CzIPN instead of 4DPAIPN	27
6	DMF instead of DMSO	trace
7	MeCN instead of DMSO	49
8	Na ₂ C ₂ O ₄ or K ₂ C ₂ O ₄ instead of H ₂ C ₂ O ₄ /TMG	trace
9	(ⁿ Bu ₄ N) ₂ C ₂ O ₄ instead of H ₂ C ₂ O ₄ /TMG	56
10	Et ₃ N or DIPEA instead of H ₂ C ₂ O ₄ /TMG	0
11	HCO ₂ H instead of H ₂ C ₂ O ₄	0
12	green LEDs (λ = 525 nm) instead of blue LEDs	47
13	red LEDs (λ = 640 nm) instead of blue LEDs	0
14	heat to 80 °C in the dark	0
15	no 4DPAIPN	0

photocatalysts:

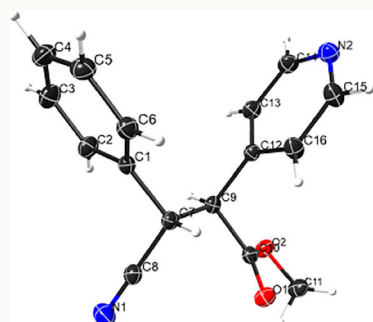
4DPAIPN: R = NPh₂
 4CzIPN: R = carbazole



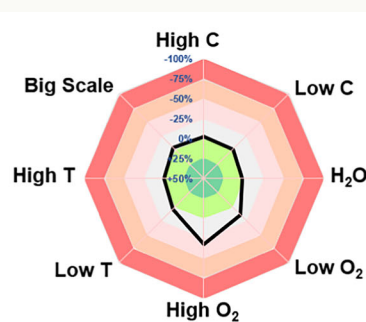
[Ru(bpy)₃](PF₆)₂



[Ir(ppy)₂(dtbbpy)](PF₆): R¹ = R² = H
 [Ir(dF(CF₃)ppy)₂(dtbbpy)](PF₆):
 R¹ = F, R² = CF₃



X-ray structure of 3aa
 CCDC 2414276



reaction sensitivity screening

LED light-emitting diode, TMG 1,1,3,3-tetramethylguanidine, DIPEAN, *N*-diisopropylethylamine.

^astandard conditions: **1a** (0.2 mmol), **2a** (0.5 mmol), H₂C₂O₄ (0.5 mmol), TMG (0.5 mmol), 4DPAIPN (1 mol%), DMSO (2 mL), argon atmosphere, 30 W blue LEDs (λ_{max} = 456 nm), rt, 90 min.

^byield was determined by ¹H NMR spectroscopy analysis with diphenylacetone (DPA) as an internal standard.

^cisolated yield in parentheses with a 1.17:1 diastereomeric ratio (d.r.).

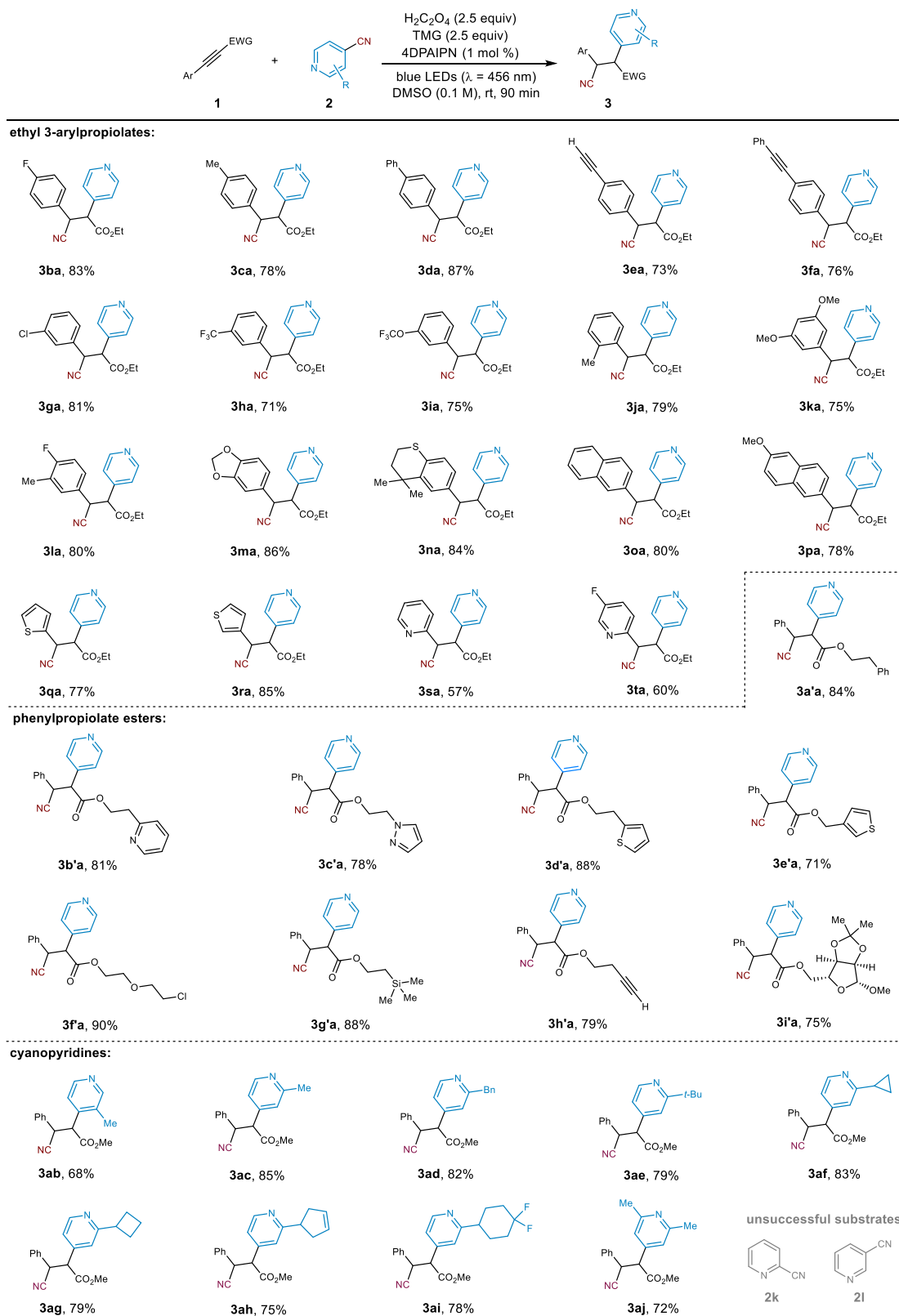
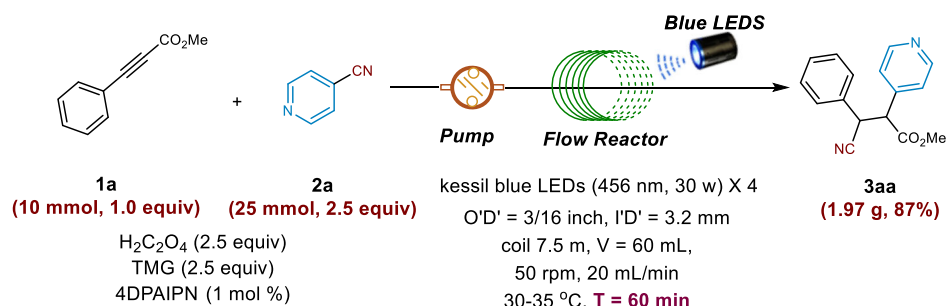
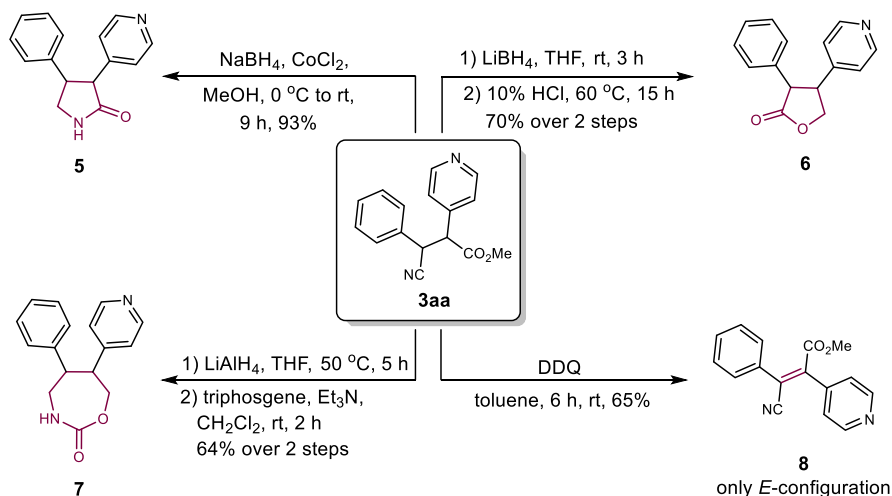


Fig. 2 | Substrate scope for the streamlined dual-FGT reaction. Reaction conditions: **1** (0.2 mmol), **2** (0.5 mmol), H₂C₂O₄ (0.5 mmol), TMG (0.5 mmol), 4DPAIPN (1 mol %), DMSO (2 mL), argon atmosphere, 30 W blue LEDs (λ_{max} = 456 nm), rt, 90 min. Isolated yields with a diastereomeric ratio (d.r.) ranging from 1:1 to 2:1. The ratio was determined by analysis of the crude ¹H NMR spectra. Refer to the characterization of products in Supplementary Information for details.

90 min. Isolated yields with a diastereomeric ratio (d.r.) ranging from 1:1 to 2:1. The ratio was determined by analysis of the crude ¹H NMR spectra. Refer to the characterization of products in Supplementary Information for details.

a Gram-scale synthesis using a circulating-flow reactor.**b Further transformations of the product 3aa.****Fig. 3 | Gram-scale synthesis and product transformations. a** Gram-scale reaction using a circulating-flow reactor. **b** Further transformations of the product **3aa**.

reduction potentials: 2-cyanopyridine ($E_{\text{p}/2}(\mathbf{2k}/\mathbf{2k}^{\bullet-}) = -1.87$ V vs SCE) and 3-cyanopyridine ($E_{\text{p}/2}(\mathbf{2l}/\mathbf{2l}^{\bullet-}) = -1.92$ V vs SCE), compared to that of 4-cyanopyridine ($E_{\text{p}/2}(\mathbf{2a}/\mathbf{2a}^{\bullet-}) = -1.70$ V vs SCE) (Supplementary Fig. 5). This led to preferential reduction of alkyne **1a** ($E_{\text{p}/2}(\mathbf{1a}/\mathbf{1a}^{\bullet-}) = -1.78$ V vs SCE) instead of **2k** or **2l**, preventing the crucial radical addition step and ultimately resulting in a complex reaction mixture. Overall, the broad applicability of both arylpropiolate esters **1** and 4-cyanopyridines **2**, bearing diverse substitution patterns and functional groups, underscores the potential of our methodology for late-stage functionalization of pharmaceuticals and natural products.

Flow synthesis and product transformations

To demonstrate the synthetic utility of this method, a gram-scale reaction of **1a** with **2a** was performed using an in-house circulating-flow reactor^{51,61}, yielding 1.97 g of product **3aa** in 87% yield (Fig. 3a). Compared to the batch reaction, our circulating-flow synthesis not only resolved the issues of low light penetration resulting from the poor solubility of oxalates but also significantly enhanced efficiency by cutting the reaction time to just 60 min. The usage of the nitrile and pyridine motifs were demonstrated by several transformations of **3aa**, as shown in Fig. 3b. Treatment of **3aa** with NaBH_4 in the presence of CoCl_2 led to γ -lactam **5** through chemo-selective reduction of the nitrile group followed by lactamization⁶². Reduction of the ester group of **3aa** with LiBH_4 , followed by lactonization under HCl/MeOH conditions, furnished lactone **6**⁶³. Alternatively, **3aa** was reduced by LiAlH_4 to form a 1,4-amino alcohol, which was then treated with triphosgene to afford the oxazolidinone **7**^{64,65}. In addition to these reductive transformations, oxidation of **3aa** with DDQ efficiently afforded the all-carbon tetrasubstituted alkene **8** with exclusive *E*-selectivity⁶⁶. These efficient constructions of pharmaceutical motifs from the product **3aa**

highlights the rich potential of this protocol in the preparation of bioactive molecules.

Mechanistic studies

To gain insight into the reaction mechanisms, several control experiments were performed. A light on/off experiment showed that continuous exposure to visible-light was essential for the reaction to occur (Supplementary Fig. 4). Radical trapping experiments with common radical scavengers, such as 2,2,6,6-tetramethyl-piperidine-1-oxyl (TEMPO) and butylated hydroxytoluene (BHT), yielded no desired products, indicating the involvement of radical intermediates in the reaction (see the radical inhibition experiments in Supplementary Information for details). To further elucidate the underlying photocatalytic mechanisms, we recorded time-resolved spectra in conjunction with steady-state spectral analysis (Fig. 4 and Supplementary Figs. 6–12) for photocatalyst 4DPAIPN (PC), both alone and in mixtures with the substrates (**1a**, **2a**, $\text{H}_2\text{C}_2\text{O}_4$, and/or $\text{C}_2\text{O}_4^{2-}$) under photoexcitation.

Electron transfer quenching studies of $^1\text{PC}^*/^3\text{PC}^*$ by $\text{C}_2\text{O}_4^{2-}$

The steady-state fluorescence quenching experiments reveal that the singlet excited state of PC ($^1\text{PC}^*$) can be efficiently quenched by $\text{C}_2\text{O}_4^{2-}$. From the Stern–Volmer plot (Fig. 4a, e) quenching rate constant (k_q) of $5.4 \times 10^9 \text{ M}^{-1} \text{ s}^{-1}$ is derived, indicating that the quenching of $^1\text{PC}^*$ by $\text{C}_2\text{O}_4^{2-}$ is highly efficient and approaches diffusion-controlled limits. Furthermore, ns time-resolved spectroscopy demonstrates that the triplet state of PC ($^3\text{PC}^*$) is also efficiently quenched by $\text{C}_2\text{O}_4^{2-}$ with a rate constant of $3.4 \times 10^8 \text{ M}^{-1} \text{ s}^{-1}$ (Fig. 4b, c, and e). In contrast, the presence of **1a**, **2a**, and/or $\text{H}_2\text{C}_2\text{O}_4$ neither affects the emission intensity of $^1\text{PC}^*$ nor the evolution of $^3\text{PC}^*$ (Fig. 4d and Supplementary

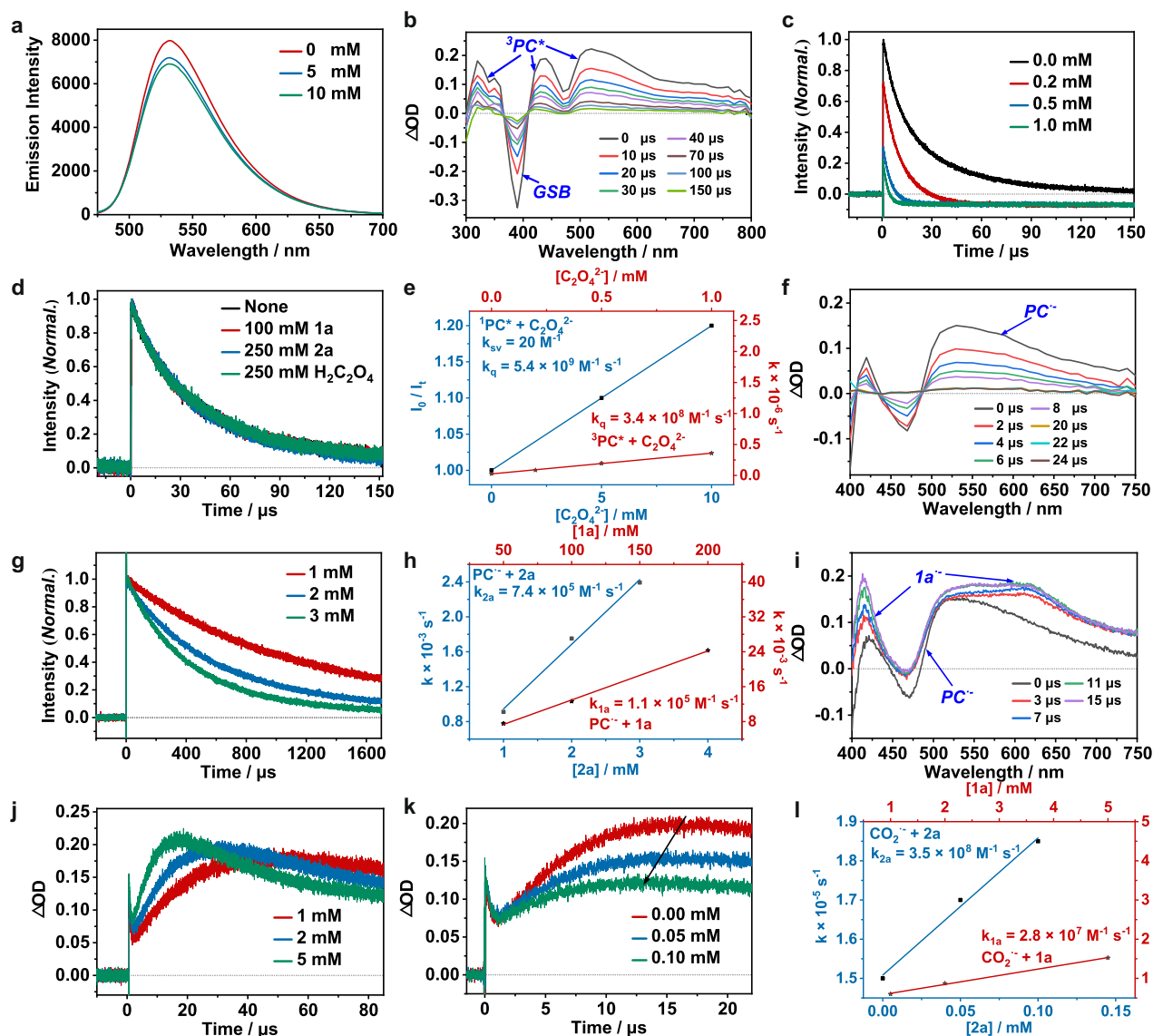


Fig. 4 | Reaction mechanism study with time-resolved transient absorption spectroscopy. **a** Steady-state emission spectra for $^1\text{PC}^*$ at different concentrations of $\text{C}_2\text{O}_4^{2-}$. **b** Transient absorption spectra for $^3\text{PC}^*$. **c** Decay traces at 450 nm for $^3\text{PC}^*$ at different concentrations of $\text{C}_2\text{O}_4^{2-}$. **d** Decay traces at 530 nm for $^3\text{PC}^*$ alone, and $^3\text{PC}^*$ in the presence of 100 mM **1a**, 250 mM **2a**, or 250 mM $\text{H}_2\text{C}_2\text{O}_4$. **e** Stern-Volmer plots for $^1\text{PC}^* + \text{C}_2\text{O}_4^{2-}$ (blue) and $^3\text{PC}^* + \text{C}_2\text{O}_4^{2-}$ (red). **f** Transient absorption spectra

for $\text{PC}^- + 250 \text{ mM } \mathbf{2a}$. **g** Decay traces at 520 nm for PC^- at different concentrations of **2a**. **h** Stern-Volmer plots for $\text{PC}^- + \mathbf{1a}$ (red) and $\text{PC}^- + \mathbf{2a}$ (blue). **i** Transient absorption spectra for $\text{CO}_2^{\cdot-} + 5 \text{ mM } \mathbf{1a}$. **j** Kinetics traces at 420 nm for $\text{CO}_2^{\cdot-} + \mathbf{1a}$ at different concentrations. **k** Kinetics traces at 420 nm for $\text{CO}_2^{\cdot-} + 5 \text{ mM } \mathbf{1a}$ at different concentrations of **2a**. **l** Stern-Volmer plots for $\text{CO}_2^{\cdot-} + \mathbf{1a}$ (red) and $\text{CO}_2^{\cdot-} + \mathbf{2a}$ (blue).

Fig. 8), indicating that these substrates do not quench $^1\text{PC}^*$ nor $^3\text{PC}^*$. These results demonstrate that the photocatalytic cycle is initiated by the quenching of both $^1\text{PC}^*$ and $^3\text{PC}^*$ by $\text{C}_2\text{O}_4^{2-}$. Additionally, ns-TA spectra reveal that the reaction between $^1\text{PC}^*/^3\text{PC}^*$ and $\text{C}_2\text{O}_4^{2-}$ efficiently generates PC^- . This radical anion is characterized by two positive bands around 420 nm and around 520 nm, along with a broad, featureless absorption extending up to 750 nm (Fig. 4f and Supplementary Fig. 9). The formation of PC^- provides direct evidence for an electron transfer quenching mechanism, thermodynamically favorable as confirmed by ΔG^0 calculations (Supplementary Table 4).

Monitoring the quenching of PC^- by **1a** and **2a**

The electron transfer from $\text{C}_2\text{O}_4^{2-}$ to $^1\text{PC}^*/^3\text{PC}^*$ results in the formation of PC^- and $\text{C}_2\text{O}_4^{\cdot-}$. The open-shell $\text{C}_2\text{O}_4^{\cdot-}$ intermediate is expected to rapidly extrude CO_2 , producing the highly reductive $\text{CO}_2^{\cdot-}$ radical anion ($\text{CO}_2^{\cdot-}$) ($E_{1/2}(\text{CO}_2/\text{CO}_2^{\cdot-}) = -2.22 \text{ V vs SCE}$)⁶⁷. After elucidating that the photocatalytic cycle begins with electron transfer from $\text{C}_2\text{O}_4^{2-}$ to

$^1\text{PC}^*/^3\text{PC}^*$ and subsequently identifying PC^- as the observed spectral species, we explored the possible reactions for $\text{PC}^- + \mathbf{1a}$ and $\text{PC}^- + \mathbf{2a}$, respectively. As depicted in Supplementary Fig. 10, PC^- remains stable on the millisecond timescale. In contrast, upon adding **2a**, the decay of PC^- was significantly accelerated, exhibiting a mono-exponential behavior (Fig. 4f,g). Linear fitting of the measured pseudo-first-order rate constants against **2a** concentration yields a second-order rate constant of $7.4 \times 10^5 \text{ M}^{-1} \text{ s}^{-1}$ (Fig. 4h).

The complete quenching of PC^- by **2a** along with the complete recovery of ground-state bleach of PC at 470 nm (Fig. 4f) suggests that the quenching corresponds to the regeneration of PC via electron transfer from PC^- to **2a**. The TD-DFT calculated spectrum for the reduction species of **2a** ($\mathbf{2a}^{\cdot-}$) exhibits minimal absorption in the detected spectral region, accounting for the transient spectral evolution back to zero baseline (Supplementary Fig. 12). Note that the reported reduction potentials for PC ($E_{p/2}(\text{PC}/\text{PC}^-) = -1.65 \text{ V vs SCE}$)⁶⁸ and **2a** ($E_{p/2}(\mathbf{2a}/\mathbf{2a}^{\cdot-}) = -1.70 \text{ V vs SCE}$). The comparable reduction

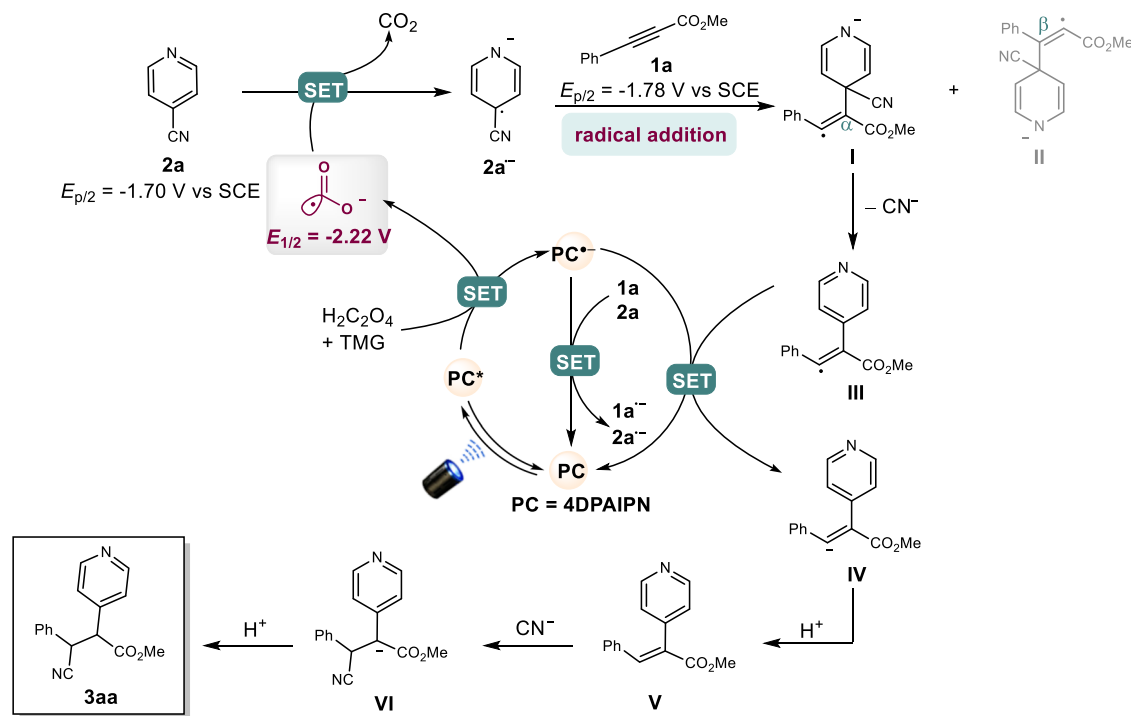


Fig. 5 | Plausible photocatalytic mechanisms. A plausible reaction mechanism for the photocatalytic streamlined dual-functional group transfer.

potential indicates that the driving force for the electron transfer from PC^- to **2a** is weak, which accounts for the relatively modest rate of $7.4 \times 10^5 \text{ M}^{-1} \text{ s}^{-1}$ for the reaction of **2a** with PC^- .

The coexisting $CO_2^{\cdot-}$ in the solution also reacts with **1a** (as will be discussed later), thereby complicating the analysis of $PC^- + 1a$ reaction. To clarify the possible reaction between $PC^- + 1a$, we designed a control experiment in which PC^- is generated by reducing $^1PC^*/^3PC^*$ with DIPEA and then quenched by **2a** or **1a** (Supplementary Fig. 11). In this way, a second-order rate constant of $5.8 \times 10^5 \text{ M}^{-1} \text{ s}^{-1}$ for the reaction $PC^- + 2a$ was obtained, consistent with the value of $7.4 \times 10^5 \text{ M}^{-1} \text{ s}^{-1}$ measured in $PC + C_2O_4^{2-} + 2a$ system (Fig. 4h). Furthermore, it was found that PC^- can also be quenched by **1a** via an electron transfer mechanism with a second-order rate constant of $1.1 \times 10^5 \text{ M}^{-1} \text{ s}^{-1}$ (Fig. 4h and Supplementary Fig. 11).

Monitoring the reduction of **1a** and **2a** with $CO_2^{\cdot-}$

As shown in Fig. 4i, introducing additional **1a** (5 mM) to the $PC/C_2O_4^{2-}$ system significantly changes the transient spectra. Within 15 μs , the intensity of the negative band around 470 nm decreases, while the intensity of the positive band around 420 nm increase, together with the buildup of a broad band around 620 nm. These changes correspond to the reaction between $PC^-/CO_2^{\cdot-} + 1a$. Given the rate of $PC^- + 1a$ ($1.1 \times 10^5 \text{ M}^{-1} \text{ s}^{-1}$) and the added concentration of **1a** (5 mM), the reaction of $PC^- + 1a$ is expected to occur on the millisecond timescale, ruling out its involvement in the initial 15 μs spectral evolution. Thus, the observed changes are attributed to the reaction $CO_2^{\cdot-} + 1a$ through electron transfer, forming reduced **1a** (**1a** $^{\cdot-}$) and CO_2 . TD-DFT calculation indicates that **1a** $^{\cdot-}$ exhibits a strong, broad absorption from 400 to 800 nm, with a peak around 515 nm (Supplementary Fig. 12), supporting the assignment of spectral evolution within 15 μs to **1a** $^{\cdot-}$ formation. Hence, the spectrum at 15 μs reflects the combined contributions of the positive absorption signals of PC^- and **1a** $^{\cdot-}$, along with the ground-state bleaching of PC. By monitoring **1a** $^{\cdot-}$ formation at 420 nm, a second-order rate constant for $CO_2^{\cdot-} + 1a$ of $2.8 \times 10^7 \text{ M}^{-1} \text{ s}^{-1}$ is determined through linear fitting of the measured pseudo-first-order rate constants versus **1a** concentration (Fig. 4j, l). In addition, **2a** is also anticipated to quench the highly reductive $CO_2^{\cdot-}$ through electron

transfer. As shown in Fig. 4k, the kinetic curves for the formation of **1a** $^{\cdot-}$ show that, with the increasing of added **2a** concentration, the amount of formed **1a** $^{\cdot-}$ as reflected by the plateau gradually decreases, while the overall formation process accelerates. This confirms that **2a** can effectively compete with **1a** for the quenching reaction with $CO_2^{\cdot-}$. By applying the differential rate equation for parallel reactions to analyze changes in 420 nm kinetics with varying concentrations of **2a**, we obtained a second-order rate constant of $3.5 \times 10^8 \text{ M}^{-1} \text{ s}^{-1}$ for $CO_2^{\cdot-} + 2a$ (Fig. 4k, l, and Supplementary Fig. 13), which is more competitive than $CO_2^{\cdot-} + 1a$.

Proposed reaction mechanism

Based on kinetic data (Fig. 4h, l), the quenching of PC^- and $CO_2^{\cdot-}$ by **2a** is predominant over that by **1a** owing to the significantly higher rate constants of **2a** compared to **1a** (5–7 times higher for PC^- and 10 times higher for $CO_2^{\cdot-}$) and the 2.5-fold higher concentration of **2a** in the reaction system. Thus, the decay of PC^- and $CO_2^{\cdot-}$ primarily corresponds to the formation of **2a** $^{\cdot-}$, while much less amount of **1a** $^{\cdot-}$ is produced. Without significant formation of **1a** $^{\cdot-}$, the potential radical coupling of **2a** $^{\cdot-}$ with **1a** $^{\cdot-}$ to form the product **3aa**, is unlikely to be the dominant pathway. Furthermore, the calculated energies of the two products from the radical coupling process do not support the experimentally observed regioselectivity, which favors α -pyridylation over the β -pyridylation product (Supplementary Fig. 14). This apparent contradiction further reinforces the conclusion that the radical coupling mechanism shown in Supplementary Fig. 14 is not the primary pathway. On the other hand, the abundant formation of **2a** $^{\cdot-}$ most likely triggers a radical addition process as illustrated in Fig. 5. Irradiation of PC with blue LEDs generates the excited $^1PC^*/^3PC^*$, followed by a single electron transfer (SET) process with $C_2O_4^{2-}$ to yield PC^- and $CO_2^{\cdot-}$, alongside the release of CO_2 . Both $CO_2^{\cdot-}$ and PC^- are quenched by **2a** to yield **2a** $^{\cdot-}$, with PC^- returning to PC, completing the catalytic cycle. Subsequently, **2a** $^{\cdot-}$ undergoes regioselective radical addition with **1a** to yield α -pyridylation intermediate **I**. This is supported by DFT calculations, which demonstrate that the pathway leading to the α -pyridylation intermediate **I** is more favorable than that leading to the β -pyridylation intermediate **II**, both in terms of the stability of the

reaction intermediates and the reaction kinetic barrier. This regioselectivity aligns well with prior literature precedent, where the crucial radical additions to arylpropiolates proceeded through α -position attack to form more stabilized benzylic-type radical intermediates^{69–71}.

Given that the quenching efficiency of $PC^{\cdot-}$ by the substrates **1a** and **2a** is much lower than that of $CO_2^{\cdot-}$, and considering the continuous irradiation of the system, $PC^{\cdot-}$ is expected to be abundant in the reaction mixture. This allows the vinyl radical intermediate **III**, generated from the α -pyridylation intermediate **I** by the release of the cyanide ion (CN^-), to accept an electron from $PC^{\cdot-}$, producing the alkenyl anion intermediate **IV** and regenerating PC . Theoretical calculations confirm the thermodynamic feasibility of this SET process (Supplementary Fig. 16 and Table 5), while deuterium-labeling experiments using $D_2C_2O_4$ and/or D_2O provide indirect support through the significant deuterium incorporation (up to 85%) at the β -position of the ester in **3aa** (see the deuterium labeling experiments in Supplementary Information for details)^{72,73}. Following protonation of intermediate **IV**, a facile Michael addition of the CN^- to intermediate **V** and subsequent protonation yield the dual-FGT product **3aa**.

Discussion

In summary, we have developed a streamlined dual-FGT reaction under visible-light irradiation, enabling the complete incorporation of cyanopyridine into internal alkynes with excellent regioselectivity. Mechanistic studies using time-resolved spectroscopy revealed that the reaction proceeds via a photoinduced regioselective radical addition of the persistent cyanopyridine radical anion to alkynes, followed by a cooperative release and re-addition of the cyanide ion (CN^-) to furnish the pyridylcyanated products. This protocol operates under mild conditions, avoids the use of expensive transition metal catalysts, and employs cyanopyridine as a clean and safe cyanation reagent. Its excellent step- and atom-economy, along with broad functional group tolerance, make it highly promising for late-stage functionalization of bioactive molecules. Moreover, the successful demonstration of large-scale circulating-flow synthesis and subsequent product transformation underscores the practicality of this method for the efficient production of value-added pharmaceutical molecules. Beyond its synthetic utility, this work also highlights the power of time-resolved spectroscopy in elucidating photochemical reaction mechanisms and is expected to inspire further advancements in the development of green and sustainable dual-FGT reactions.

Methods

General procedure D

To a 10 mL microwave vial equipped with a magnetic stir bar, arylpropiolate ester **1** (0.2 mmol, 1.0 equiv.), cyanopyridine **2** (0.5 mmol, 2.5 equiv.), oxalic acid (0.5 mmol, 2.5 equiv.), TMG (0.5 mmol, 2.5 equiv.), 4DPAIPN (0.002 mmol, 0.01 equiv.) and DMSO (2.0 mL) were sequentially added. The reaction mixture was degassed three times via freeze-pump-thaw. Then the reactor was placed at a distance (app. 5 cm) from two 30 W 456 nm light-emitting diode (LED) lamps, stirred and irradiated at room temperature with a fan for 90 min under argon atmosphere. After completion of the reaction (by TLC analysis), it was quenched with deionized water (10 mL), and extracted with EtOAc (3 \times 10 mL). The combined organic layers were washed with brine (20 mL), dried over Na_2SO_4 , filtered, and concentrated by rotary evaporation. The residue was purified by column chromatography using hexane/EtOAc/ Et_3N (10:1:0.05 to 5:1:0.05) to afford the desired pyridylcyanated product **3**.

Data availability

The X-ray crystallographic coordinates for structure reported in this article have been deposited at the Cambridge Crystallographic Data Center (CCDC), under deposition numbers CCDC 2414276. These data can be obtained free of charge from the CCDC via www.ccdc.cam.ac.uk/data_request/cif. All data to support the conclusions are available in the main text or the Supplementary Information. The data that support the findings of this study are available from the corresponding authors upon request.

References

- Trost, B. M. On inventing reactions for atom economy. *Acc. Chem. Res.* **35**, 695–705 (2002).
- Wang, H., Tian, Y.-M. & König, B. Energy- and atom-efficient chemical synthesis with endergonic photocatalysis. *Nat. Rev. Chem.* **6**, 745–755 (2022).
- Bhawal, B. N. & Morandi, B. Catalytic transfer functionalization through shuttle catalysis. *ACS Catal.* **6**, 7528–7535 (2016).
- Rössler, S. L. et al. Pyridinium salts as redox-active functional group transfer reagents. *Angew. Chem. Int. Ed.* **59**, 9264–9280 (2020).
- Huang, H.-M., Bellotti, P., Ma, J., Dalton, T. & Glorius, F. Bifunctional reagents in organic synthesis. *Nat. Rev. Chem.* **5**, 301–321 (2021).
- Liu, J., Jiang, H.-W., Hu, X.-Q. & Xu, P.-F. Visible-light-induced alkoxypyridylation of alkenes using N-alkoxypyridinium salts as bifunctional reagents. *Org. Lett.* **26**, 3661–3666 (2024).
- Li, M. et al. Visible light-mediated organocatalyzed 1,3-aminoacylation of cyclopropane employing N-benzoyl saccharin as bifunctional reagent. *Nat. Commun.* **15**, 8930 (2024).
- Hou, J. et al. Visible-light-mediated metal-free difunctionalization of alkenes with CO_2 and silanes or C(sp³)-H alkanes. *Angew. Chem. Int. Ed.* **57**, 17220–17224 (2018).
- Jiang, H. & Studer, A. Intermolecular radical carboamination of alkenes. *Chem. Soc. Rev.* **49**, 1790–1811 (2020).
- Tu, H.-Y. et al. Enantioselective three-component fluoroalkylarylation of unactivated olefins through nickel-catalyzed cross-electrophile coupling. *J. Am. Chem. Soc.* **142**, 9604–9611 (2020).
- Wang, Y. et al. Recent advances in difunctionalization of alkenes using pyridinium salts as radical precursors. *Chem. Commun.* **58**, 3847–3864 (2022).
- Bian, K.-J. et al. Modular difunctionalization of unactivated alkenes through bio-inspired radical ligand transfer catalysis. *J. Am. Chem. Soc.* **144**, 11810–11821 (2022).
- Nakao, Y., Oda, S. & Hiyama, T. Nickel-catalyzed arylcyanation of alkynes. *J. Am. Chem. Soc.* **126**, 13904–13905 (2004).
- Li, H., Cheng, Z., Tung, C.-H. & Xu, Z. Atom transfer radical addition to alkynes and enynes: a versatile gold/photoredox approach to thio-functionalized vinylsulfones. *ACS Catal.* **8**, 8237–8243 (2018).
- Qin, J. et al. Photoinduced nickel-catalyzed homolytic C(sp³)-N bond activation of isonitriles for selective carbo- and hydrocyanation of alkynes. *J. Am. Chem. Soc.* **146**, 27583–27593 (2024).
- Lee, K., Lee, S., Kim, N., Kim, S. & Hong, S. Visible-light-enabled trifluoromethylative pyridylation of alkenes from pyridines and triflic anhydride. *Angew. Chem. Int. Ed.* **59**, 13379–13384 (2020).
- Jiang, H., Yu, X., Daniliuc, C. G. & Studer, A. Three-component aminoarylation of electron-rich alkenes by merging photoredox with nickel. *Catal. Angew. Chem. Int. Ed.* **60**, 14399–14404 (2021).
- Fan, Y., Huang, Z., Lu, Y., Zhu, S. & Chu, L. Defluorinative alkylboration of alkenes enabled by dual photoredox and copper catalysis. *Angew. Chem. Int. Ed.* **63**, e202315974 (2024).
- Monos, T. M., McAtee, R. C. & Stephenson, C. R. Arylsulfonylacetamides as bifunctional reagents for alkene aminoarylation. *Science* **361**, 1369–1373 (2018).
- Zhang, M., Zhang, J. & Oestreich, M. Photoinduced radical-ionic dihalogen transfer to carbon-carbon multiple bonds using oxime-based surrogates. *Nat. Synth.* **2**, 439–447 (2023).
- Giri, R. et al. Visible-light-mediated vicinal dihalogenation of unsaturated C-C bonds using dual-functional group transfer reagents. *J. Am. Chem. Soc.* **146**, 31547–31559 (2024).
- Oestreich, M. Transfer hydrosilylation. *Angew. Chem. Int. Ed.* **55**, 494–499 (2016).

23. Yu, J., Wu, Z. & Zhu, C. Efficient docking–migration strategy for selective radical difluoromethylation of alkenes. *Angew. Chem. Int. Ed.* **57**, 17156–17160 (2018).
24. Wu, X. & Zhu, C. Radical-mediated remote functional group migration. *Acc. Chem. Res.* **53**, 1620–1636 (2020).
25. Yu, J. et al. Metal-free radical difunctionalization of ethylene. *Chem* **9**, 472–482 (2023).
26. Moon, Y. et al. Visible light induced alkene aminopyridylation using N-aminopyridinium salts as bifunctional reagents. *Nat. Commun.* **10**, 4117 (2019).
27. Guo, S.-Y. et al. Photo-induced catalytic halopyridylation of alkenes. *Nat. Commun.* **12**, 6538 (2021).
28. Vitaku, E., Smith, D. T. & Njardarson, J. T. Analysis of the structural diversity, substitution patterns, and frequency of nitrogen heterocycles among US FDA approved pharmaceuticals: miniperspective. *J. Med. Chem.* **57**, 10257–10274 (2014).
29. Zafar, M., Atif, A., Nazar, M., Sumrra, S. & Paracha, R. Pyridine and related ligands in transition metal homogeneous catalysis. *Russ. J. Coord. Chem.* **42**, 1–18 (2016).
30. Lewis, D. E. Aleksei Yevgen'evich Chichibabin (1871–1945): a century of pyridine chemistry. *Angew. Chem. Int. Ed.* **56**, 9660–9668 (2017).
31. Miller, J. S. & Manson, J. L. Designer magnets containing cyanides and nitriles. *Acc. Chem. Res.* **34**, 563–570 (2001).
32. Fleming, F. F. & Wang, Q. Unsaturated nitriles: conjugate additions of carbon nucleophiles to a recalcitrant class of acceptors. *Chem. Rev.* **103**, 2035–2078 (2003).
33. Bhutani, P. et al. US FDA approved drugs from 2015–June 2020: a perspective. *J. Med. Chem.* **64**, 2339–2381 (2021).
34. Fleming, F. F., Yao, L., Ravikumar, P., Funk, L. & Shook, B. C. Nitrile-containing pharmaceuticals: efficacious roles of the nitrile pharmacophore. *J. Med. Chem.* **53**, 7902–7917 (2010).
35. Frolov, N. A. & Vereshchagin, A. N. Piperidine derivatives: recent advances in synthesis and pharmacological applications. *Int. J. Mol. Sci.* **24**, 2937 (2023).
36. Zhang, Y. et al. Light-induced divergent cyanation of alkynes enabled by phosphorus radicals. *Angew. Chem. Int. Ed.* **61**, e202210838 (2022).
37. Cui, K., Li, Y.-L., Li, G. & Xia, J.-B. Regio- and stereoselective reductive coupling of alkynes and crotononitrile. *J. Am. Chem. Soc.* **144**, 23001–23009 (2022).
38. McNally, A., Prier, C. K. & MacMillan, D. W. C. Discovery of an α -amino C–H arylation reaction using the strategy of accelerated serendipity. *Science* **334**, 1114–1117 (2011).
39. Cuthbertson, J. D. & MacMillan, D. W. The direct arylation of allylic sp^3 C–H bonds via organic and photoredox catalysis. *Nature* **519**, 74–77 (2015).
40. Chen, D. et al. Metal-free, intermolecular carbopyridylation of alkenes via visible-light-induced reductive radical coupling. *Chem. Sci.* **9**, 9012–9017 (2018).
41. Cao, J. et al. Perfluoroalkylative pyridylation of alkenes via 4-cyanopyridine-boryl radicals. *Chem. Sci.* **10**, 2767–2772 (2019).
42. Zheng, W. et al. Light-promoted arylsilylation of alkenes with hydrosilanes. *Org. Lett.* **24**, 7145–7150 (2022).
43. Shen, J., Li, J., Chen, M. & Chen, Y. Photocatalyst-free, metal-free, visible light-induced thiolation/pyridylation of styrenes using an electron donor–acceptor complex as a bifunctional reagent. *Org. Chem. Front.* **10**, 1166–1172 (2023).
44. Feng, L.-M., Liu, S., Tu, Y.-H., Rui, P.-X. & Hu, X.-G. Radical deoxygenative three-component reaction of alcohols, aryl alkenes, and cyanopyridines. *Org. Lett.* **26**, 6225–6229 (2024).
45. Tang, D.-D., Wang, Y.-Z., Liu, C., Xia, Y. & Li, Y. Photoredox-catalyzed amino-radical-transfer-mediated three-component alkylarylation of alkenes. *Org. Lett.* **26**, 6477–6481 (2024).
46. Zhang, Z. et al. Visible-light-induced acylative pyridylation of styrenes. *Org. Lett.* **26**, 4727–4732 (2024).
47. Tong, S., Li, K., Ouyang, X., Song, R. & Li, J. Recent advances in the radical-mediated decyanative alkylation of cyano(hetero)arene. *Green. Synth. Catal.* **2**, 145–155 (2021).
48. Chao, F., Yang, H.-B. & Fang, Y. Photoredox-catalyzed decyanative radical cross-coupling reactions of aromatic nitriles. *ChemCatChem* **16**, e202301281 (2024).
49. Yoshida, Y., Okada, W., Takada, K., Nakamura, S. & Yasukawa, N. Photocatalytic decyanative radical addition based on cyano group transfer mediated by amine-ligated boryl radicals. *Org. Lett.* **27**, 7236–7241 (2025).
50. Wu, Z., Wu, M., Zhu, K., Wu, J. & Lu, Y. Photocatalytic coupling of electron-deficient alkenes using oxalic acid as a traceless linchpin. *Chem* **9**, 978–988 (2023).
51. Tong, X. et al. Photocatalytic reductive functionalization of aryl alkynes via alkyne radical anions. *ACS Catal.* **14**, 9283–9293 (2024).
52. Gao, B., Deng, D., Huang, D. & Sun, X. Recent advances in the tandem difunctionalization of alkynes: mechanism-based classification. *Synthesis* **53**, 3522–3534 (2021).
53. Ghosh, S., Chakraborty, R. & Ganesh, V. Dual functionalization of alkynes utilizing the redox characteristics of transition metal catalysts. *ChemCatChem* **13**, 4262–4298 (2021).
54. Liu, W. & Kong, W. Ni-Catalyzed stereoselective difunctionalization of alkynes. *Org. Chem. Front.* **7**, 3941–3955 (2020).
55. Li, H., Tian, X., Dang, Q.-Q., Zhang, J. & Wen, Z.-K. Overcoming electron bias in hydroarylation of phenylpropionic acid derivatives to enable highly reversed regio- and stereoselectivity via steric and transient post addition coordination. *ACS Catal.* **14**, 9985–9992 (2024).
56. Corpas, J., Mauleón, P., Arrayás, R. G. & Carretero, J. C. Transition-metal-catalyzed functionalization of alkynes with organoboron reagents: new trends, mechanistic insights, and applications. *ACS Catal.* **11**, 7513–7551 (2021).
57. Boyarskiy, V. P., Ryabukhin, D. S., Bokach, N. A. & Vasilyev, A. V. Alkenylation of arenes and heteroarenes with alkynes. *Chem. Rev.* **116**, 5894–5986 (2016).
58. Biffis, A., Tubaro, C. & Baron, M. Advances in transition-metal-catalysed alkyne hydroarylations. *Chem. Rec.* **16**, 1742–1760 (2016).
59. Yamamoto, Y. Synthesis of heterocycles via transition-metal-catalyzed hydroarylation of alkynes. *Chem. Soc. Rev.* **43**, 1575–1600 (2014).
60. Pitzer, L., Schäfers, F. & Glorius, F. Rapid assessment of the reaction-condition-based sensitivity of chemical transformations. *Angew. Chem. Int. Ed.* **58**, 8572–8576 (2019).
61. Liu, C. et al. High-Speed circulation flow platform facilitating practical large-scale heterogeneous photocatalysis. *Org. Process Res. Dev.* **28**, 1964–1970 (2024).
62. Nagata, K. et al. Asymmetric synthesis and catalytic activity of 3-methyl- β -proline in enantioselective anti-Mannich-type reactions. *J. Org. Chem.* **78**, 7131–7136 (2013).
63. Kusakabe, T., Kato, K., Motodate, S., Takaishi, S. & Akita, H. Conversion of optically active hydrindanone to (+)-bakkenolide-A. *Chem. Pharm. Bull.* **56**, 1436–1437 (2008).
64. Li, C., Yu, R., Cai, S.-Z. & Fang, X. Highly diastereoselective synthesis of polysubstituted cyclopropanecarbonitriles via palladium-catalyzed cyanoesterification of cyclopropenes. *Org. Lett.* **25**, 5128–5133 (2023).
65. Zhong, Z. et al. Visible-light-promoted enantioselective acylation and alkylation of aldimines enabled by 9-fluorenone electron-shuttle catalysis. *J. Am. Chem. Soc.* **146**, 20401–20413 (2024).
66. Hudkins, R. L. et al. Mixed-lineage kinase 1 and mixed-lineage kinase 3 subtype-selective dihydronaphthyl[3,4-a]pyrrolo[3,4-c]carbazole-5-ones: optimization, mixed-lineage kinase 1 crystallography, and oral in vivo activity in 1-methyl-4-phenyltetrahydropyridine models. *J. Med. Chem.* **51**, 5680–5689 (2008).

67. Koppenol, W. & Rush, J. Reduction potential of the carbon dioxide/carbon dioxide radical anion: a comparison with other C1 radicals. *J. Phys. Chem.* **91**, 4429–4430 (1987).
68. Alektiar, S. N. & Wickens, Z. K. Photoinduced hydrocarboxylation via thiol-catalyzed delivery of formate across activated alkenes. *J. Am. Chem. Soc.* **143**, 13022–13028 (2021).
69. Hong, Y. et al. Tetrafluoroisopropylation of alkenes and alkynes enabled by photocatalytic consecutive difluoromethylation with CF₂HSO₂Na. *Nat. Commun.* **15**, 5685 (2024).
70. Le, S. et al. 3+2 Cycloaddition of alkyl aldehydes and alkynes enabled by photoinduced hydrogen atom transfer. *Nat. Commun.* **13**, 4734 (2022).
71. Gu, Z., Jia, R., Zeng, T., Zheng, H. & Zhu, G. Photocatalytic [3+2] cycloaddition of alkyl/aryl iodides and internal alkynes by merging halogen and hydrogen atom transfer. *Chin. J. Chem.* **42**, 2329–2334 (2024).
72. Zhou, W., Dmitriev, I. A. & Melchiorre, P. Reductive cross-coupling of olefins via a radical pathway. *J. Am. Chem. Soc.* **145**, 25098–25102 (2023).
73. Wang, H., Gao, Y., Zhou, C. & Li, G. Visible-light-driven reductive carboxylation of styrenes with CO₂ and aryl halides. *J. Am. Chem. Soc.* **142**, 8122–8129 (2020).

Acknowledgements

The authors are grateful for the financial support from National Natural Science Foundation of China (22461045 [X.T.], 22473014 [J.J.], 22371200 [J.W.], and 21933005 [H.S.]), the National Key R&D Program of China (No. 2022YFA1505400 [J.J.]), Yunnan Revitalization Talent Support Program (Young Talent Project [X.T.]), Natural Science Foundation of Yunnan Province (202201AT070205 [X.T.]), and the Ministry of Education (MOE) of Singapore (T2EP10224-0005 [J.W.]). We also thank the Advanced Analysis and Measurement Center of Yunnan University for HRMS and NMR analysis.

Author contributions

J.W. and H.S. supervised the project and coordinated the collaboration. X.T. conceived the research and performed the experiments. J.J. and Y.L. conducted mechanistic investigations using time-resolved spectroscopy and theoretical calculations. H.Y., G.W., and D.T. participated in starting material preparation and flow analysis. M.Y. carried out HRMS measurements and data analysis. X.T., J.J., H.T.A., H.S., and J.W. wrote the manuscript. All authors contributed to the discussion of the manuscript.

Competing interests

The authors declare no competing interests.

Additional information

Supplementary information The online version contains supplementary material available at <https://doi.org/10.1038/s41467-025-64029-2>.

Correspondence and requests for materials should be addressed to Hongmei Su or Jie Wu.

Peer review information *Nature Communications* thanks Ahmad Masarwa, Peng Yang and the other anonymous reviewer(s) for their contribution to the peer review of this work. A peer review file is available.

Reprints and permissions information is available at <http://www.nature.com/reprints>

Publisher's note Springer Nature remains neutral with regard to jurisdictional claims in published maps and institutional affiliations.

Open Access This article is licensed under a Creative Commons Attribution-NonCommercial-NoDerivatives 4.0 International License, which permits any non-commercial use, sharing, distribution and reproduction in any medium or format, as long as you give appropriate credit to the original author(s) and the source, provide a link to the Creative Commons licence, and indicate if you modified the licensed material. You do not have permission under this licence to share adapted material derived from this article or parts of it. The images or other third party material in this article are included in the article's Creative Commons licence, unless indicated otherwise in a credit line to the material. If material is not included in the article's Creative Commons licence and your intended use is not permitted by statutory regulation or exceeds the permitted use, you will need to obtain permission directly from the copyright holder. To view a copy of this licence, visit <http://creativecommons.org/licenses/by-nc-nd/4.0/>.

© The Author(s) 2025